



Fluctuation theorem anomaly in a point-vortex fluidRama Sharma ¹, Tapio P. Simula,¹ and Andrew J. Groszek ^{2,3}¹*Optical Sciences Centre, Swinburne University of Technology, Melbourne, Victoria 3122, Australia*²*ARC Centre of Excellence for Engineered Quantum Systems, School of Mathematics and Physics, University of Queensland, St. Lucia, Queensland 4072, Australia*³*ARC Centre of Excellence in Future Low-Energy Electronics Technologies, School of Mathematics and Physics, University of Queensland, Saint Lucia, Queensland 4072, Australia*

(Received 7 August 2023; accepted 28 June 2024; published 24 July 2024)

The second law of thermodynamics posits that in closed macroscopic systems the rate of entropy production must be positive. However, small systems can exhibit negative entropy production over short timescales, seemingly in contradiction with this law. The fluctuation theorem quantitatively connects these two limits, predicting that entropy-producing trajectories become exponentially dominant as the system size and measurement time are increased. Here, we explore the predictions of the fluctuation theorem for a fluid of point vortices, in which the long-range Lorentz-like interactions and existence of negative-absolute-temperature states provide an intriguing test bed for the theorem. Our results suggest that while the theorem broadly holds even at negative absolute temperatures, the form of the interactions inherent in the vortex matter lead to anomalously large entropy production over short time intervals. The predictions of the fluctuation theorem are only fully recovered when sufficient noise is introduced to the dynamics to overwhelm the vortex-vortex interactions.

DOI: [10.1103/PhysRevA.110.013321](https://doi.org/10.1103/PhysRevA.110.013321)**I. INTRODUCTION**

The second law of thermodynamics states that in a closed macroscopic system entropy will only ever increase [1–3]. However, as identified by Loschmidt [4], a question arises regarding how such irreversible behavior can emerge from the microscopic equations of motion, which are themselves reversible. In mathematical terms, why is it that a system's phase-space trajectory has a preferred direction towards a higher-entropy state when the corresponding time-reversed trajectory would appear to be equally likely to occur? Fluctuation theorems (FTs) provide one approach for resolving this paradox. They predict that a physical system can always exhibit both entropy-producing and entropy-reducing trajectories through phase space but that the latter are exponentially suppressed as the system size or evolution time is increased. These theorems therefore bridge the gap between the reversible microscopic and irreversible macroscopic dynamics and recover the familiar second-law behavior in the thermodynamic limit.

FTs can be categorized into two broad classes: Evans-Searles-type FTs, which predict the statistics of the entropy produced in systems perturbed from equilibrium by a constant driving [5–10], and Crooks-type FTs, which predict the statistics of work fluctuations in systems with time-dependent driving [11,12]. Importantly, these theorems are not restricted to equilibrium systems, providing one of the few analytical thermodynamic predictions valid in the nonequilibrium regime. A wealth of experimental verification now exists for both forms of FT [13–20], cementing their importance in our understanding of statistical physics.

In this work we consider the statistical properties of a fluid of point vortices. This system consists of a collection

of pointlike vortex “particles” that interact with each other via long-range Coulombic forces. Unlike massive particles, these vortex particles experience a velocity perpendicular to this interaction force, analogous to the magnetic Lorentz force on a charge. Point vortices were first considered as a toy model for two-dimensional (2D) fluids but more recently have been found to accurately describe the dynamics of quantized vortices in 2D superfluid Bose-Einstein condensates [21–28]. One remarkable feature of this system is its ability to exhibit negative-absolute-temperature states in any bounded container, as identified by Onsager [29]. In this negative-temperature regime, the vortices tend to form same-sign clusters [22,23,30,31], maximizing the kinetic energy of the flow field while reducing the configurational entropy. These negative-temperature states have now been realized experimentally in ultracold gases [25,26] and, more recently, in exciton-polariton condensates [32].

Here, we investigate the applicability of the Evans-Searles FT to the point-vortex fluid, given its unusual features of long-range, Lorentz-like interaction forces and negative absolute temperatures. In analogy with Ref. [13], we consider a driving scheme in which one vortex is dragged by an external potential through the system, which is otherwise in equilibrium at a chosen temperature. Our results indicate that while the theorem seems largely unaffected by the sign of the temperature, the unusual form of the vortex-vortex interactions does appear to give rise to anomalously large entropy production over short timescales, leading to a disagreement with the FT prediction. However, over longer timescales the FT—and, in turn, the second law of thermodynamics—is recovered.

The rest of this paper is organized as follows. Section II describes the system setup and numerical methods employed. Section III formally defines the Evans-Searles FT and outlines

our method for applying it to the point-vortex fluid. In Sec. IV, we discuss our main results. We explore how the FT predictions are affected by the temperature of the system, the finite system size, and noise added to the vortex dynamics. Finally, in Sec. V we conclude and discuss potential future research directions.

II. METHODS

A. Point-vortex system

We model a system of N_v point vortices in a square geometry of side length L , with periodic boundaries in both directions. We fix $N_v = 100$ unless otherwise stated. If we write the position of vortex i as (x_i, y_i) and its circulation as $\Gamma_i = s_i \Gamma_0$ (with $s_i = \pm 1$ and Γ_0 being a unit of circulation), the pseudo-Hamiltonian for such a system can be expressed as [33]

$$H = -\frac{\rho}{2} \sum_{i=1}^{N_v} \sum_{j \neq i}^{N_v} \Gamma_i \Gamma_j G(x_{ij}, y_{ij}), \quad (1)$$

where

$$G(x_{ij}, y_{ij}) = \sum_{n=-\infty}^{\infty} \ln \left(\frac{\cosh[(2\pi x_{ij}/L) - 2\pi n] - \cos(2\pi y_{ij}/L)}{\cosh(2\pi n)} \right) - 2\pi (x_{ij}/L)^2 \quad (2)$$

and ρ is the bulk value of the 2D superfluid mass density. Here, $x_{ij} = x_i - x_j$ (with similar notation for y_{ij}). We restrict our analysis to the neutral vortex system, for which there are an equal number of clockwise- and counterclockwise-circulating vortices.

The conservative equations of motion for the vortices [which we denote with the superscript (0)] are given by Hamilton's equations,

$$\rho \Gamma_i \dot{x}_i^{(0)} = \partial H / \partial y_i, \quad (3)$$

$$\rho \Gamma_i \dot{y}_i^{(0)} = -\partial H / \partial x_i,$$

which for the Hamiltonian (1) reduce to

$$\dot{x}_i^{(0)} = \frac{\pi}{L} \sum_{j \neq i}^{N_v} \left(\Gamma_j \sum_{n=-\infty}^{\infty} \frac{\sin(2\pi y_{ij}/L)}{\cosh[(2\pi x_{ij}/L) - 2\pi n] - \cos(2\pi y_{ij}/L)} \right), \quad (4)$$

$$\dot{y}_i^{(0)} = -\frac{\pi}{L} \sum_{j \neq i}^{N_v} \left(\Gamma_j \sum_{n=-\infty}^{\infty} \frac{\sin(2\pi x_{ij}/L)}{\cosh[(2\pi y_{ij}/L) - 2\pi n] - \cos(2\pi x_{ij}/L)} \right).$$

For the purposes of testing the fluctuation theorem in this system, we modify the dynamical model by adding a driving term in analogy with an earlier work [13]. Specifically, we attach one vortex to a harmonic trapping potential, which is translated at a constant velocity $\mathbf{v}_{\text{trap}} = v_{\text{trap}} \hat{\mathbf{e}}_x$ across the system, where $\hat{\mathbf{e}}_x$ is the x -directional unit vector. In addition to the forces arising from interactions with other vortices, this “test” vortex thus experiences a restoring force $\mathbf{F}_{\text{restoring}} = -K(\mathbf{r}_{\text{test}} - \mathbf{r}_{\text{trap}})$ towards the center of the translating harmonic trap. Here, \mathbf{r}_{test} (\mathbf{r}_{trap}) is the location of the test vortex (trap center), and K is a parameter that determines the stiffness of the trap. We assume that this force is realized by a dissipative Gaussian laser beam, which locally depletes the superfluid mass density from its bulk value ρ , pulling the test vortex towards its center with a velocity $\dot{\mathbf{r}}_{\text{restoring}} = \mathbf{F}_{\text{restoring}} / \rho \Gamma_0$ [34–38]. We account for this additional velocity by modifying the equations of motion (4) such that

$$\dot{x}_i = \dot{x}_i^{(0)} - k(x_{\text{test}} - x_{\text{trap}}) \delta_{i, \text{test}}, \quad (5)$$

$$\dot{y}_i = \dot{y}_i^{(0)} - k(y_{\text{test}} - y_{\text{trap}}) \delta_{i, \text{test}},$$

where we have defined the spring constant $k = K / \rho \Gamma_0$. Numerically, we implement the restoring force in such a way that the dynamics are “unwrapped” with respect to the periodic boundaries: when the trap moves infinitesimally from $x = +L/2$ to $x = -L/2$, the force on the vortex does not change in strength or direction.

A schematic of our system setup is shown in Fig. 1(a), with vortices (antivortices) shown as blue (red) circles and the harmonic trap depicted by the pink shaded region with the test vortex captured inside of it. We track the trajectory of the test vortex during the dynamics and use it to investigate the FT predictions for the vortex system (see Sec. III). In Figs. 1(b) and 1(c), we plot the horizontal displacement δx of the test vortex (blue curve) relative to the trap center (pink line) as a function of simulation time for two different spring constants k . As expected, the test vortex is able to drift farther from the trap center for smaller k [Fig. 1(b)]. In all our simulations, the

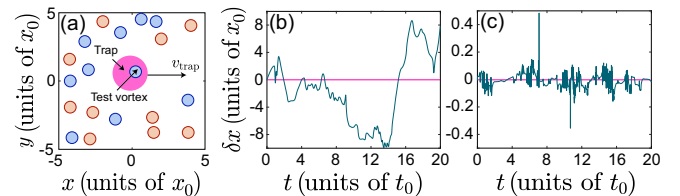


FIG. 1. (a) Schematic of our system with 10 positive-circulation (blue) and 10 negative-circulation (red) point vortices in a doubly periodic square geometry. The harmonic trapping potential (indicated by the pink shaded circle) moves at a constant speed v_{trap} in the positive x direction, dragging the test vortex through the system. (b) and (c) show the horizontal deflection δx (blue line) of the test vortex relative to the trap center (pink line) as a function of time for trap spring constants $k = 0.5 t_0^{-1}$ and $k = 100 t_0^{-1}$, respectively. In both cases, $v_{\text{trap}} = 0.3 x_0 / t_0$.

dynamics are initialized with the trap at the location of the test vortex (hence, $\delta x = 0$ at $t = 0$), and the trap is translated at a velocity of $v_{\text{trap}} = 0.3x_0/t_0$. Here and throughout this work, we express length, time, and energy in units of $x_0 = L/10$, $t_0 = x_0^2/\Gamma_0$, and $\varepsilon_0 = \rho\Gamma_0x_0^2/t_0$, respectively.

B. Numerical implementation

In the following, we explore the behavior of the vortex system as a function of the (inverse) vortex temperature β [29]. We do this by sampling the initial states for our dynamical simulations from a canonical ensemble at fixed β . As in earlier works [24,39,40], we achieve this using a Markov chain Monte Carlo method. Briefly, every step in the Markov chain involves randomly selecting one vortex from the configuration, attempting to move it a small distance in a random direction, and then deciding whether to accept the move. The probability of accepting a given move is given by the Metropolis rule, $\min\{1, \exp(-\beta\Delta H)\}$, where ΔH is the change in the energy (1) that would be produced by the move. To avoid singular behavior, we reject all moves that cause any two vortices to be separated by less than $0.0016x_0$.

For a given choice of temperature, we perform a total of 10^6 Markov-chain steps. Following an initial burn-in of 10^5 steps, we sample 1000 microstates separated by intervals of 900 steps to ensure minimal correlations between sampled states. We then use these microstates as our ensemble of initial conditions at the chosen β and evolve each in time by numerically integrating Eq. (4) with the additional trapping potential described in the previous section. The dynamical simulations are conducted using a fourth-order Runge-Kutta method with 6000 numerical time steps over an integration time of $40t_0$.

III. FLUCTUATION THEOREM

The Evans-Searles fluctuation theorem predicts that, for a nonequilibrium finite system, the second law of thermodynamics will be violated over short timescales [5,6]. Mathematically, the theorem states that over a time interval τ , the probability $P(\sigma_\tau)$ of observing a phase-space trajectory that *produces* entropy σ_τ is related to the probability $P(-\sigma_\tau)$ of observing a trajectory that *consumes* an equivalent amount of entropy via the expression

$$\frac{P(-\sigma_\tau)}{P(\sigma_\tau)} = \exp(-\sigma_\tau). \quad (6)$$

Since σ_τ is an extensive quantity, this ratio becomes increasingly small as either the system size or the time interval τ is increased, and hence, the second law is recovered in the thermodynamic limit [13]. The derivation of this expression assumes that the system under consideration is time reversible, ergodic, and at fixed energy when no driving is applied [9,41]. These conditions should all be well satisfied for this point-vortex system [42].

Here, we consider an integrated form of the FT [13,43],

$$\frac{P(\sigma_\tau < 0)}{P(\sigma_\tau > 0)} = \langle \exp(-\sigma_\tau) \rangle_{\sigma_\tau > 0}, \quad (7)$$

where the angular brackets on the right-hand side (RHS) denote an average over all trajectories that produce entropy. The

left-hand side (LHS) of Eq. (7) may be measured by taking the ratio of the number of entropy-consuming ($\sigma_\tau < 0$) and entropy-generating ($\sigma_\tau > 0$) trajectories over time interval τ .

Our primary goal is to investigate the applicability of Eq. (7) for the case of point vortices by comparing the two sides of Eq. (7). We define the entropy σ_τ produced (or consumed) over a time τ by the translating trap as the ratio of the work W_τ done by the translating trap to the thermal energy $k_B T_p$:

$$\sigma_\tau = -\frac{W_\tau}{k_B T_p}. \quad (8)$$

Here, T_p is an ambient ‘‘phonon’’ temperature, which we treat as a free parameter in our simulations because the point-vortex model does not account for the dynamics of phonon degrees of freedom that would be present in a superfluid. We calculate the work W_τ done by the trap over time $\tau = t_f - t_i$ as an integral of the scalar product between the trapping force $\mathbf{F}_{\text{restoring}}$ acting on the test vortex and the trap translation velocity \mathbf{v}_{trap} . Hence, Eq. (8) becomes

$$\sigma_\tau = \alpha \int_{t_i}^{t_f} d\mathbf{s} \mathbf{v}_{\text{trap}} \cdot \mathbf{F}_{\text{restoring}}, \quad (9)$$

where we have defined the phonon (inverse) temperature $\alpha = 1/(k_B T_p)$. Since the trap is translating at a constant velocity, this expression will result in entropy production ($\sigma_\tau > 0$) whenever the test vortex is behind the trap and entropy consumption ($\sigma_\tau < 0$) when the test vortex gets pushed ahead of the trap due to interactions with other vortices in the system.

IV. RESULTS

A. Effect of the vortex temperature

We first consider a test of the FT as a function of the vortex temperature. To this end, we have run dynamical simulations for a range of initial temperatures spanning from the Berezinskii-Kosterlitz-Thouless (BKT) transition temperature $\beta_{\text{BKT}} = 8\pi/\rho\Gamma_0^2$, at which the vortices and antivortices pair strongly to form dipoles [44–46], to the Einstein-Bose-condensation transition temperature $\beta_{\text{EBC}} = -16\pi/\rho\Gamma_0^2 N_v$, where the vortices arrange into same-sign clusters to maximize the energy [39,47–49]. In the following, we scale all positive temperatures β_+ by β_{BKT} and all negative temperatures β_- by β_{EBC} [24,26,40].

In Fig. 2 we present histograms of the entropy production σ_τ at three vortex temperatures, $\beta_+ = 1$, $\beta_+ = 0$, and $\beta_- = -1$. For each temperature, we have produced histograms using both a short time interval, $\tau \approx 0.007t_0$ [Figs. 2(a)–2(c)], and a longer interval $\tau = 40t_0$ [Figs. 2(d)–2(f)]. The dashed vertical line in each panel denotes $\sigma_\tau = 0$. In Figs. 2(a)–2(c), the distributions are almost symmetric about $\sigma_\tau = 0$, indicating that entropy-consuming and -producing trajectories are approximately equally likely for such short time intervals. By contrast, for the longer integration times shown in Figs. 2(d)–2(f), the histograms become skewed towards $\sigma_\tau > 0$, reflecting the tendency for entropy to be produced over long times, on average. Ultimately, for sufficiently long time intervals, entropy-producing trajectories should become overwhelmingly dominant with almost vanishing probability

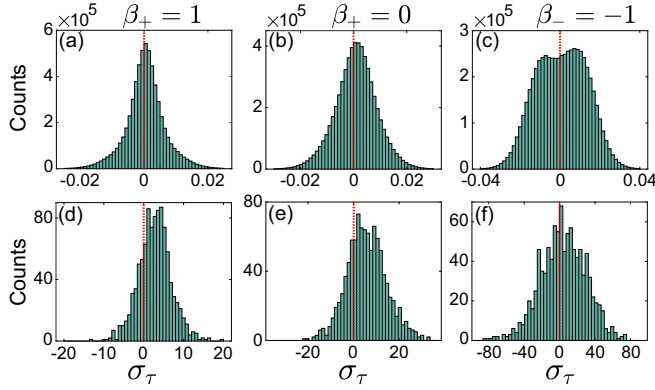


FIG. 2. Histograms of the dimensionless entropy production σ_τ . The three columns correspond to inverse vortex temperatures $\beta_+ = 1$, $\beta_+ = 0$ and $\beta_- = -1$, from left to right. The measurement intervals are (a)–(c) $\tau \approx 0.007t_0$ and (d)–(f) $\tau = 40t_0$, and the dashed red vertical line in each panel indicates the location of $\sigma_\tau = 0$. Each histogram is produced from an ensemble of 1000 computational trajectories, and we use every possible window of length τ in each simulation. The total sample sizes for these histograms are therefore 1000×6000 for (a)–(c) and 1000×1 for (d)–(f).

of entropy-consuming trajectories, in accordance with the second law of thermodynamics. It can also be seen in Fig. 2 that as the vortex temperature shifts from positive to negative, the entropy distribution widens. This is presumably due to the stronger flow fields produced by the vortex clusters, which

push the test vortex further from the trap center, in turn giving rise to larger restoring forces.

Using these entropy distributions, we can test the FT prediction in Eq. (7). For the temperatures β we have considered, we independently measure the LHS and RHS of Eq. (7) for varying time intervals in the range $0.007t_0 \lesssim \tau \lesssim 40t_0$. The results are presented in Fig. 3. Figures 3(a)–3(e) depict example initial-vortex configurations at five inverse temperatures, $\beta_+ = \{1, 0.5, 0\}$ and $\beta_- = \{-0.5, -1\}$, demonstrating the transition from dipole pairing to same-sign clustering as β is reduced. The trap position is shown as a pink asterisk, which coincides with the test vortex at time $t = 0$. Figures 3(f)–3(j) show the resulting FT curves corresponding to each temperature as a function of τ , with the red (teal) line corresponding to the LHS (RHS) of Eq. (7). Note that the right-hand side involves the free parameter α , defined in Eq. (9). We treat α as an optimization parameter and set it equal to the value for which the mean-square error between the two curves is minimized over all τ . In all cases, it can be seen that the two curves start near unity and tend towards zero with increasing τ , in broad agreement with the predictions of the fluctuation theorem. However, as β is reduced, the timescale required for entropy production to dominate over entropy consumption increases. This suggests that at negative temperatures, our driving protocol becomes much less efficient at producing entropy and instead continues to produce almost equal numbers of entropy-producing and entropy-reducing trajectories even for large τ [this is also reflected in the near symmetry of the histogram in Fig. 2(f)]. Regardless, Eq. (7) still appears to be broadly satisfied for $\beta < 0$, suggesting that the

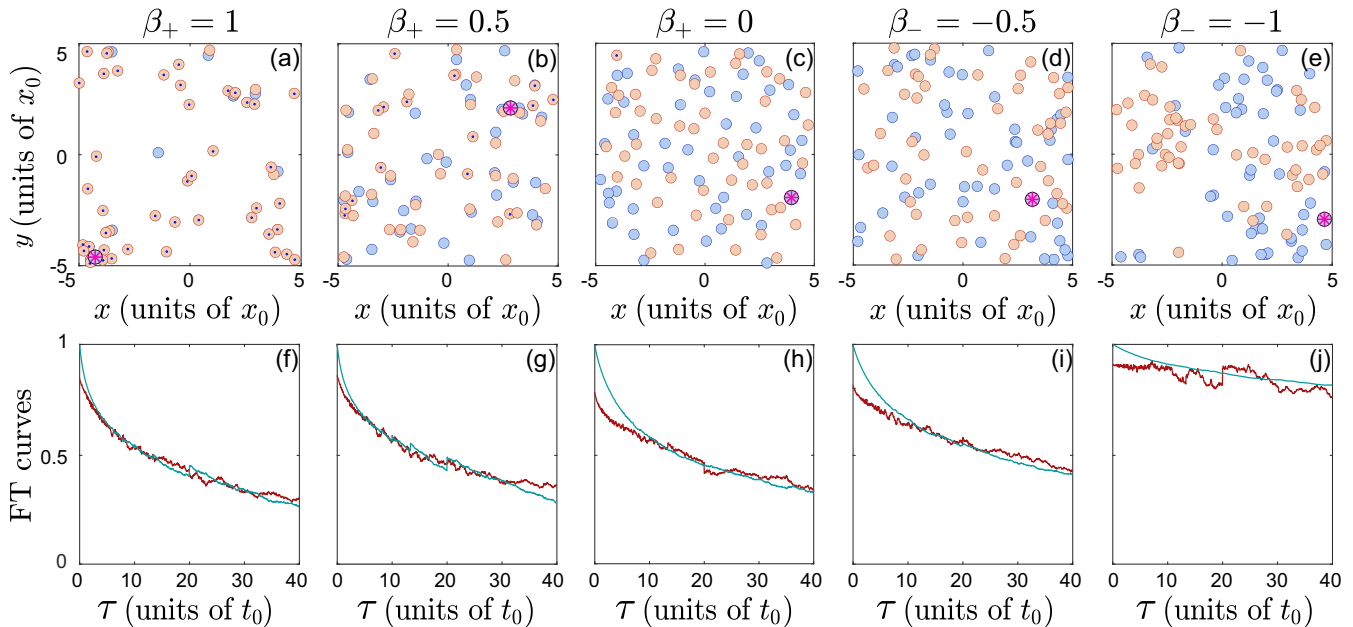


FIG. 3. (a)–(e) Initial vortex configurations and (f)–(j) the corresponding fluctuation-theorem (FT) curves for inverse vortex temperatures $\beta_+ = \{1, 0.5, 0\}$ and $\beta_- = \{-0.5, -1\}$. The blue and red markers in the top row represent the vortex and antivortex locations, respectively. A blue dot inside a red marker indicates the presence of a vortex directly beneath the antivortex. The pink asterisk indicates the trap location at $t = 0$, which coincides with the initial position of the test vortex. The bottom row shows the number ratio (red curves) of entropy-consuming ($\sigma_\tau < 0$) to entropy-producing ($\sigma_\tau > 0$) trajectories as per the left-hand side of Eq. (7), together with the right-hand side of Eq. (7), $\langle \exp(-\sigma_\tau) \rangle_{\sigma_\tau > 0}$ (teal curves). Each curve has been averaged over 1000 simulations of a system with $N_v = 100$. The trap parameters are $v_{\text{trap}} = 0.3x_0/t_0$ and $k = 100t_0^{-1}$.

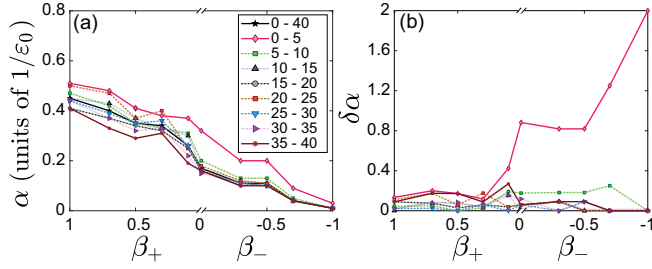


FIG. 4. (a) The fitted phonon inverse temperature $\alpha = 1/(k_B T_p)$ as a function of the vortex temperature β . At each value of β , we extracted α using nine different fitting time intervals, as indicated in the legend. (b) The relative deviation $\delta\alpha = |\alpha - \tilde{\alpha}|/\tilde{\alpha}$ between each fitted α and the value $\tilde{\alpha}$ obtained from the fit to the full time window $\tau = [0-40]t_0$. The color coding is as in (a).

fluctuation theorem still holds even in this exotic temperature regime.

Curiously, however, Figs. 3(f)–3(j) all show a slight disagreement between the two FT curves for small time intervals τ . Specifically, the LHS of Eq. (7) (red curves) is lower than the RHS for small τ , indicating that even for the shortest intervals $P(\sigma_\tau > 0) > P(\sigma_\tau < 0)$ in this system. Expressed another way, our point-vortex system never produces equal numbers of entropy-producing and entropy-reducing trajectories, even for arbitrarily small τ . The value of τ at which the two curves first coincide increases weakly as β is reduced, suggesting that this effect is at least partially dependent on the vortex temperature. We explore this discrepancy further in the following sections.

First, however, we investigate how the value of the fitted phonon temperature α varies as a function of the vortex temperature β . To ensure that its value is robust to the chosen window of τ over which we choose to fit the two sides of Eq. (7), we measure α from fits to nine time intervals: $\tau \in \{0-40, 0-5, 5-10, 10-15, 15-20, 20-25, 25-30, 30-35, 35-40\}t_0$. The results are shown in Fig. 4(a). Interestingly, there is a near-linear relationship between α and β (note that this trend continues across $\beta = 0$ despite the difference in scaling for $\beta > 0$ and $\beta < 0$). However, α appears to be strictly positive, unlike β . Figure 4(b) shows the relative deviation $\delta\alpha = |\alpha - \tilde{\alpha}|/\tilde{\alpha}$ of each measured α from the value $\tilde{\alpha}$ extracted over the full fitting time interval $[0-40]t_0$. Fitting to any interval beginning after $\tau \approx 10t_0$ gives $\alpha \approx \tilde{\alpha}$ (i.e., near-zero deviation). However, the strong deviation for the earliest time interval $[0-5]t_0$ clearly quantifies the disagreement between the two FT curves for small τ , which becomes more significant as β is reduced towards increasingly negative temperatures.

B. Finite-size effects

The discrepancy between the two sides of Eq. (7) identified in Figs. 3 and 4 may be due to the finite size of our numerical simulation domain, in which case it should diminish as the system size increases and the thermodynamic limit is approached. To test this, we explore the effects of varying both the trap strength k and the vortex number N_v . Larger k values prevent the test vortex from traversing large distances across the domain, effectively making the (periodic) boundaries

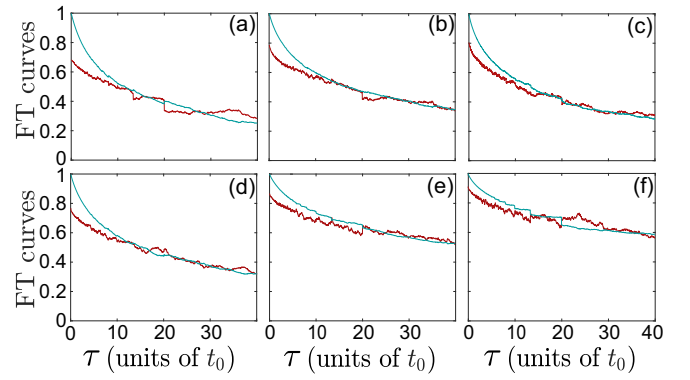


FIG. 5. Tests of finite-size effects at $\beta_+ = 0$. The top row shows the FT curves for a system with $N_v = 100$ vortices with trap strengths (a) $k = 7t_0^{-1}$, (b) $k = 100t_0^{-1}$, and (c) $k = 1000t_0^{-1}$. In the bottom row, the vortex number is (d) $N_v = 50$, (e) $N_v = 200$, and (f) $N_v = 400$, with fixed trap strength $k = 100t_0^{-1}$. In each frame, the red (teal) curve corresponds to the left (right) side of Eq. (7), as in Fig. 3. In all cases, the trap speed is fixed at $v_{\text{trap}} = 0.3x_0/t_0$, and α values were obtained by fitting to the full time interval (see Sec. IV A).

appear farther away. Larger N_v values, on the other hand, result in higher vortex densities, which essentially correspond to larger system sizes (except for an overall change in timescales since the mean vortex velocity also increases).

Figure 5 shows the results of our finite-size tests, with the vortex temperature fixed at $\beta_+ = 0$. Figures 5(a)–5(c) show the FT curves for $N_v = 100$ with trap strengths $k = 7t_0^{-1}$, $k = 100t_0^{-1}$, and $k = 1000t_0^{-1}$, respectively. The deviation at small τ does appear to decrease as k is increased, although the LHS of Eq. (7) (red curve) shows little indication of approaching unity at $\tau \approx 0$. It therefore does not appear that increasing k is sufficient to completely eliminate the discrepancy. Figures 5(d)–5(f) show the FT curves for fixed trap strength $k = 100t_0^{-1}$ and vortex numbers $N_v = 50$, $N_v = 200$, and $N_v = 400$, respectively. The two curves appear to converge as N_v is increased, suggesting that the observed discrepancy may disappear as N_v is increased further. Nonetheless, it is interesting that this disagreement exists even in finite-size systems, and hence, we wish to explore its origin.

C. Effect of vortex-vortex interactions

Point vortices are unusual in that their interactions are inherently long range and the corresponding forces give rise to perpendicular motion. To investigate the importance of these features of our system, here, we introduce noise to the motion of the vortices, allowing us to effectively tune out the long-range interactions by overwhelming them with local fluctuations. Physically, this noise plays the role of the phonon bath in which the vortices would be immersed in a superfluid Bose-Einstein condensate. From the perspective of the test vortex, there are therefore two contributions to the environment it is moving through: a coherent part arising from long-range interactions and an incoherent part corresponding to the noise. To explore the interplay between these two effects, we study three scenarios: (1) noise added to all vortices *except* the test vortex, (2) noise added to all vortices, including the test vortex, and (3) noise added to the test vortex when no

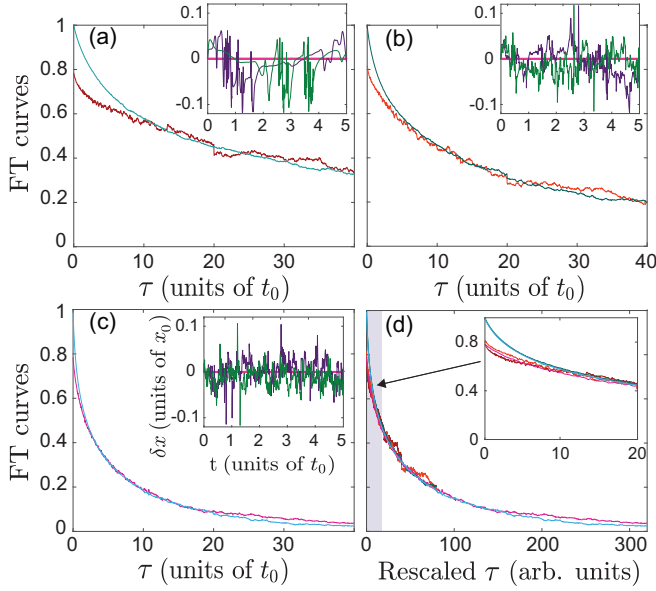


FIG. 6. FT curves at vortex temperature $\beta_+ = 0$ with noise added to the all vortices except the test vortex. The first three panels correspond to noise amplitudes (a) $\Delta = 0$, (b) $\Delta = 100x_0/t_0$, and (c) $\Delta = 200x_0/t_0$. As in Fig. 3, the red and teal curves correspond to the left- and right-hand sides of Eq. (7), respectively. The insets of (a)–(c) each show two examples of the vortex deflection as in Figs. 1(b) and 1(c). The axis labels for the insets in (a) and (b) are the same as for the inset in (c) but have been omitted for visual clarity. (d) shows a collapse of the three datasets in (a)–(c), achieved by rescaling the time axis by multiplicative factors 1, 2, and 8, respectively. The inset of (d) shows a magnified view highlighting the small- τ behavior, with the axes being the same as for the main frame. In all cases, $v_{\text{trap}} = 0.3x_0/t_0$, $k = 100t_0^{-1}$, and $N_v = 100$.

other vortices are present. We implement the noise by adding an additional term, $\delta \mathbf{v}_i = \eta_i \hat{\mathbf{e}}_x + \zeta_i \hat{\mathbf{e}}_y$, to the velocity \mathbf{v}_i of vortex i in Eq. (4). The velocity increments η_i and ζ_i are randomly generated each time step from a uniform distribution within the range $[-\Delta, \Delta]$, where Δ is the chosen noise amplitude.

We first explore case 1, in which noise is added only to the environment vortices. In Figs. 6(a)–6(c), we show the analysis of the two sides of Eq. (7) with noise amplitudes $\Delta = \{0, 100, 200\}x_0/t_0$, respectively. Each panel includes an inset showing the deflection of the test-vortex position from the trap center (horizontal pink line) as a function of time from two example simulations at the corresponding value of Δ (purple and green curves). At the outset it appears in Figs. 6(b) and 6(c) that the early time deviation has been mitigated by the noise when compared with Fig. 6(a). However, a careful analysis of Fig. 6(c) reveals that for very short time intervals the deviation persists. To make this observation clearer, Fig. 6(d) reproduces the data in Figs. 6(a)–6(c) with the time axis rescaled by factors of 1, 2, and 8, respectively. Under this rescaling, the data collapse, and hence, increasing Δ in this scenario is effectively equivalent to reducing the timescale of the dynamics. In the inset of Fig. 6(d), we focus on the small- τ limit, clearly revealing that the deviation is present in all three cases. It therefore appears that no amount of noise added to the environment vortices could achieve agreement

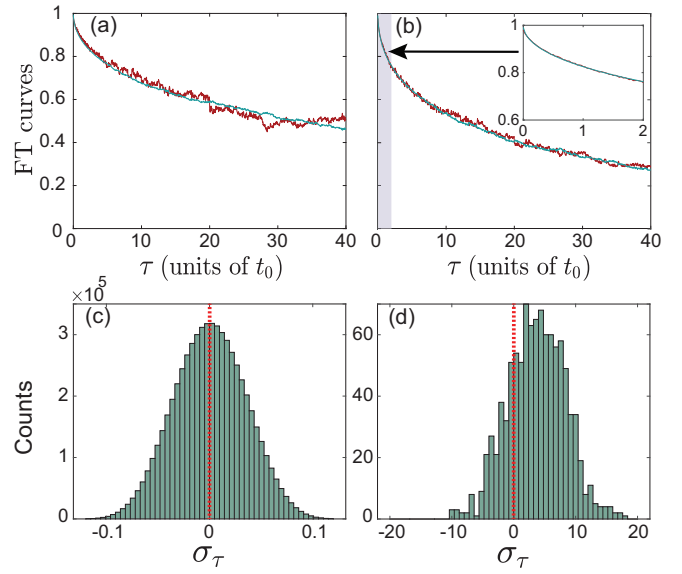


FIG. 7. Fluctuation-theorem results with noise added to the test vortex. (a) FT curves for a system of $N_v = 100$ vortices at temperature $\beta_+ = 0$, with noise of amplitude $\Delta = 200x_0/t_0$ added to all vortices, including the test vortex. (b)–(d) correspond to a system with only the test vortex present and added noise with amplitude $\Delta = 100x_0/t_0$. (b) FT curves, with the inset showing an average over 10 000 simulations analyzed for small τ , as indicated by the purple shaded region. (c) and (d) show histograms of the dimensionless entropy production σ_τ for time intervals $\tau = 0.007t_0$ (1000×6000 samples) and $\tau = 40t_0$ (1000×1 samples), respectively. In all cases, $v_{\text{trap}} = 0.3x_0/t_0$, and $k = 100t_0^{-1}$.

in this scenario. One possible explanation for this is that the vortex-vortex interactions are causing the deviation, meaning that the two curves would coincide only if local fluctuations were also added to the test vortex.

We next turn to case 2, in which noise is also added to the test vortex. This situation most closely resembles a true Bose-Einstein condensate, in which the phonon bath will affect all vortices equivalently. We explore a range of noise amplitudes Δ and find that for $\Delta \lesssim 100x_0/t_0$, the deviation between the two sides of Eq. (7) at small τ persists. However, for noise amplitudes greater than this, the discrepancy is no longer visible. An example case with $\Delta = 200x_0/t_0$ is shown in Fig. 7(a). In this case, the left-hand side of Eq. (7) does approach unity as $\tau \rightarrow 0$, meaning that there are equal numbers of entropy-producing and entropy-consuming trajectories in this limit. This supports the interpretation that the intervortex interactions are responsible for the small τ anomaly because at these amplitudes the noise is much stronger than the mean velocity \bar{v} arising from long-range interactions, which is of the order of $\bar{v} \sim \Gamma_0/\bar{d} \sim 1x_0/t_0$ for our setup, where $\bar{d} \sim L/N_v^{1/2}$ is the mean distance between vortices.

Finally, we examine case 3, in which only the test vortex is present and vortex-vortex interactions are entirely absent. This scenario trivially reduces to Brownian motion of the vortex in the trap, which more closely resembles earlier works on the fluctuation theorem [13]. The results of this test are presented in Figs. 7(b)–7(d). Figure 7(b) shows the two sides of Eq. (7), with the inset displaying data averaged over a

larger ensemble. Evidently, the agreement is excellent for all τ . This result can also be verified directly from the histogram in Fig. 7(c), which shows that the entropy production is distributed symmetrically around zero for the shortest time interval, $\tau = 0.007t_0$, demonstrating an equal probability of positive- and negative-entropy trajectories. This in contrast to the $\tau = 40t_0$ case shown in Fig. 7(c), where the histogram is strongly skewed towards entropy production. Our results are therefore consistent with the explanation that the long-range vortex-vortex interactions are responsible for the short time-interval deviations from the fluctuation theorem prediction of Eq. (7).

V. CONCLUSIONS

We studied the fluctuation theorem in the context of a 2D vortex fluid by considering the driven dynamics of an ensemble of point vortices in a doubly periodic square domain at both positive and negative absolute vortex temperatures. We found, in general, good agreement with the predictions of the FT. However, for short time intervals, we consistently observed anomalous deviations from the FT in our numerical simulations. These deviations were found to be persistent with respect to a change in the finite system parameters, although they did appear to decrease as the vortex density was increased. Only when the long-range vortex-vortex interactions were either overwhelmed by noise or eliminated completely was full agreement with the fluctuation theorem recovered. Hence, we conclude that some aspect of the long-range vortex-vortex interactions in this system plausibly leads to anomalous deviations from the FT.

The question of which specific feature of the interactions is responsible for the FT anomaly remains. Previous work in the context of dusty plasmas demonstrated that the FT can still hold in the presence of Coulombic interactions [50], suggesting that the long-range nature alone is not sufficient to cause the observed deviations. However, vortex-vortex interactions also have a Lorentz-like character, which may be a key difference in our system. We leave a more careful decoupling of these properties for future work.

Our observations call for further investigations into Onsager's statistical hydrodynamics of point vortices and into the role of long-range interactions in nonequilibrium systems more generally. In particular, it is known that nonequilibrium fluctuations in systems with short-range particle interactions readily generate long-range spatial correlations [51]. By contrast, our results point to a situation where long-range particle interactions appear to produce anomalous local entropy fluctuations. Further elucidation of our observations may potentially have an impact on studies of quantum viscosity and nonequilibrium transport phenomena in superfluids.

ACKNOWLEDGMENTS

This research was supported by the Australian Government through the Australian Research Council (ARC) Future Fellowship (Grant No. FT180100020), the ARC Centre of Excellence for Engineered Quantum Systems (Grant No. CE170100009), and the ARC Centre of Excellence in Future Low-Energy Electronics Technologies (Grant No. CE170100039).

-
- [1] L. Boltzmann, in *Theoretical Physics and Philosophical Problems* (Springer, Dordrecht, The Netherlands, 1974), pp. 13–32.
 - [2] C. J. Adkins, *Equilibrium Thermodynamics* (Cambridge University Press, Cambridge, 1983).
 - [3] P. Attard, *Non-equilibrium Thermodynamics and Statistical Mechanics: Foundations and Applications* (Oxford University Press, Oxford, 2012).
 - [4] J. Loschmidt, *Sitzungsber. Kais. Akad. Wiss. Wien, Math. Naturwiss. Classe, II. Abteilung* **73**, 128 (1876).
 - [5] D. J. Evans, E. G. D. Cohen, and G. P. Morriss, *Phys. Rev. Lett.* **71**, 2401 (1993).
 - [6] D. J. Evans and D. J. Searles, *Phys. Rev. E* **50**, 1645 (1994).
 - [7] G. Gallavotti and E. G. D. Cohen, *J. Stat. Phys.* **80**, 931 (1995).
 - [8] G. Gallavotti and E. G. D. Cohen, *Phys. Rev. Lett.* **74**, 2694 (1995).
 - [9] D. J. Evans and D. J. Searles, *Adv. Phys.* **51**, 1529 (2002).
 - [10] E. Sevick, R. Prabhakar, S. R. Williams, and D. J. Searles, *Annu. Rev. Phys. Chem.* **59**, 603 (2008).
 - [11] C. Jarzynski, *Phys. Rev. Lett.* **78**, 2690 (1997).
 - [12] G. E. Crooks, *Phys. Rev. E* **60**, 2721 (1999).
 - [13] G. M. Wang, E. M. Sevick, E. Mittag, D. J. Searles, and D. J. Evans, *Phys. Rev. Lett.* **89**, 050601 (2002).
 - [14] J. Liphardt, S. Dumont, S. B. Smith, I. Tinoco, Jr., and C. Bustamante, *Science* **296**, 1832 (2002).
 - [15] D. Collin, F. Ritort, C. Jarzynski, S. B. Smith, I. Tinoco, Jr., and C. Bustamante, *Nature (London)* **437**, 231 (2005).
 - [16] N. Garnier and S. Ciliberto, *Phys. Rev. E* **71**, 060101(R) (2005).
 - [17] S. Schuler, T. Speck, C. Tietz, J. Wrachtrup, and U. Seifert, *Phys. Rev. Lett.* **94**, 180602 (2005).
 - [18] F. Douarche, S. Joubaud, N. B. Garnier, A. Petrosyan, and S. Ciliberto, *Phys. Rev. Lett.* **97**, 140603 (2006).
 - [19] C. Tietz, S. Schuler, T. Speck, U. Seifert, and J. Wrachtrup, *Phys. Rev. Lett.* **97**, 050602 (2006).
 - [20] Y. Utsumi, D. S. Golubev, M. Marthaler, K. Saito, T. Fujisawa, and G. Schön, *Phys. Rev. B* **81**, 125331 (2010).
 - [21] R. Navarro, R. Carretero-González, P. J. Torres, P. G. Kevrekidis, D. J. Frantzeskakis, M. W. Ray, E. Altuntaş, and D. S. Hall, *Phys. Rev. Lett.* **110**, 225301 (2013).
 - [22] T. P. Billam, M. T. Reeves, B. P. Anderson, and A. S. Bradley, *Phys. Rev. Lett.* **112**, 145301 (2014).
 - [23] T. Simula, M. J. Davis, and K. Helmerson, *Phys. Rev. Lett.* **113**, 165302 (2014).
 - [24] A. J. Groszek, M. J. Davis, D. M. Paganin, K. Helmerson, and T. P. Simula, *Phys. Rev. Lett.* **120**, 034504 (2018).
 - [25] G. Gauthier, M. T. Reeves, X. Yu, A. S. Bradley, M. A. Baker, T. A. Bell, H. Rubinsztein-Dunlop, M. J. Davis, and T. W. Neely, *Science* **364**, 1264 (2019).
 - [26] S. P. Johnstone, A. J. Groszek, P. T. Starkey, C. J. Billington, T. P. Simula, and K. Helmerson, *Science* **364**, 1267 (2019).

- [27] A. J. Groszek, P. Comaron, N. P. Proukakis, and T. P. Billam, *Phys. Rev. Res.* **3**, 013212 (2021).
- [28] M. T. Reeves, K. Goddard-Lee, G. Gauthier, O. R. Stockdale, H. Salman, T. Edmonds, X. Yu, A. S. Bradley, M. Baker, H. Rubinsztein-Dunlop, M. J. Davis, and T. W. Neely, *Phys. Rev. X* **12**, 011031 (2022).
- [29] L. Onsager, *Nuovo Cimento* **6**, 279 (1949).
- [30] M. T. Reeves, T. P. Billam, B. P. Anderson, and A. S. Bradley, *Phys. Rev. Lett.* **110**, 104501 (2013).
- [31] A. J. Groszek, T. P. Simula, D. M. Paganin, and K. Helmersen, *Phys. Rev. A* **93**, 043614 (2016).
- [32] R. Panico, P. Comaron, M. Matuszewski, A. S. Lanotte, D. Trypogeorgos, G. Gigli, M. D. Giorgi, V. Ardizzone, D. Sanvitto, and D. Ballarini, *Nat. Photon.* **17**, 451 (2023).
- [33] J. B. Weiss and J. C. McWilliams, *Phys. Fluids* **3**, 835 (1991).
- [34] P. Ao and D. J. Thouless, *Phys. Rev. Lett.* **70**, 2158 (1993).
- [35] B. Jackson, J. F. McCann, and C. S. Adams, *Phys. Rev. A* **61**, 013604 (1999).
- [36] A. J. Groszek, D. M. Paganin, K. Helmersen, and T. P. Simula, *Phys. Rev. A* **97**, 023617 (2018).
- [37] T. Simula, *Phys. Rev. A* **97**, 023609 (2018).
- [38] A nondissipative potential would produce the same force, but the resulting velocity would be perpendicular to the potential, giving rise to circular motion around the trap center.
- [39] R. N. Valani, A. J. Groszek, and T. P. Simula, *New J. Phys.* **20**, 053038 (2018).
- [40] R. Sharma and T. P. Simula, *Phys. Rev. A* **105**, 033301 (2022).
- [41] D. J. Searles and D. J. Evans, *J. Chem. Phys.* **113**, 3503 (2000).
- [42] Point vortices are typically expected to exhibit ergodic behavior in the limit of large vortex numbers (see, e.g., [52]). We therefore assume this condition is met in our system. We note that, when implementing time-reversal symmetry, the vortex signs must also be reversed to reflect the reversal of the fluid flow.
- [43] G. Ayton, D. J. Evans, and D. J. Searles, *J. Chem. Phys.* **115**, 2033 (2001).
- [44] V. L. Berezinskii, *Sov. Phys. JETP* **32**, 493 (1971).
- [45] V. L. Berezinskii, *Sov. Phys. JETP* **34**, 610 (1972).
- [46] J. M. Kosterlitz and D. J. Thouless, *J. Phys. C* **6**, 1181 (1973).
- [47] R. H. Kraichnan, *Phys. Fluids* **10**, 1417 (1967).
- [48] R. H. Kraichnan and D. Montgomery, *Rep. Prog. Phys.* **43**, 547 (1980).
- [49] J. A. Viececell, *Phys. Fluids* **7**, 1402 (1995).
- [50] C.-S. Wong, J. Goree, Z. Haralson, and B. Liu, *Nat. Phys.* **14**, 21 (2018).
- [51] P. L. Garrido, J. L. Lebowitz, C. Maes, and H. Spohn, *Phys. Rev. A* **42**, 1954 (1990).
- [52] D. G. Dritschel, M. Lucia, and A. C. Poje, *Phys. Rev. E* **91**, 063014 (2015).